

# Green's function approximation from cross-correlation of active sources in the ocean

Laura A. Brooks<sup>a)</sup> and Peter Gerstoft

*Marine Physical Laboratory, Scripps Institution of Oceanography, La Jolla, California 92093*

(Received 15 January 2009; revised 1 May 2009; accepted 2 May 2009)

Green's function approximation via ocean noise cross-correlation, referred to here as ocean acoustic interferometry, has been demonstrated experimentally for passive noise sources. Active sources offer the advantages of higher frequencies, controllability, and continuous monitoring. Experimental ocean acoustic interferometry is described here for two active source configurations: a source lowered vertically and one towed horizontally. Results are compared and contrasted with cross-correlations of passive noise. The results, in particular, differences between the empirical Green's function estimates and simulated Green's functions, are explained with reference to theory and simulations. Approximation of direct paths is shown to be consistently good for each source configuration. Secondary (surface reflection) paths are shown to be more accurate for hydrophones with a greater horizontal separation.

© 2009 Acoustical Society of America. [DOI: 10.1121/1.3143143]

PACS number(s): 43.30.Pc [RCG]

Pages: 46–55

## I. INTRODUCTION

Using passive noise, good estimates of the acoustic Green's function between two points can be determined from cross-correlation of sound in the ocean,<sup>1–6</sup> a technique referred to as ocean acoustic interferometry (OAI). This concept has been applied across a broad range of physical scales in different media including ultrasonic noise,<sup>7</sup> ambient noise in a homogeneous medium,<sup>8</sup> seismic noise,<sup>9–13</sup> moon-seismic noise,<sup>14</sup> human skeletal muscle noise,<sup>15</sup> and general fluid-solid systems.<sup>16</sup> Noise interferometry is good at obtaining the travel time part of the Green's function, and it is common to estimate both group and phase velocities.<sup>12,13</sup> Green's function estimates can be useful for inferring information about the environment through which the acoustic transmission takes place.<sup>9,14</sup> Since noise is ever-present, noise interferometry is also potentially useful for the continuous monitoring of changes in the environment.<sup>15</sup> Green's function amplitudes from noise are more difficult to extract,<sup>3</sup> as will be shown in Sec. II; however, some progress has been made in this area.<sup>17,18</sup> Noise interferometry extracts the Green's function directly from the data, which requires time-averaging while the active or passive noise builds up. A stationary environment is therefore assumed. Media can, however, be inhomogeneous (including range dependence). In fact, a more complicated environment is beneficial, as the scattering tends to create a more isotropic field.

Based on theoretical and numerical analysis,<sup>5,19,20</sup> active source interferometry has been suggested as an alternative method for Green's function estimation. Although active OAI has similar difficulties with extracting amplitude information as passive techniques, it does present a number of

advantages, including the use of higher frequencies (larger bandwidth gives sharper arrivals), controllability, and continuous monitoring. Greater knowledge of the contributing sources also means that more realistic simulated data can be produced.

To obtain an accurate representation of the Green's function, sound waves must propagate isotropically.<sup>21</sup> An active set of sources surrounding the receivers could potentially achieve this. However, only sources that emit acoustic paths passing through both receivers contribute to the Green's function.<sup>2,3</sup> These sources are all located in the end-fire plane, where *end-fire* is defined here as within the vertical plane containing both receivers (i.e., the plane defined by the vertical and horizontal arrays). Due to the technical complexity of surrounding the receivers completely, two simpler active source configurations are investigated here: (1) a source lowered through the water column at end-fire to a set of receivers, a configuration previously examined theoretically and through simulation;<sup>1,5</sup> (2) a source towed at a constant depth along the end-fire direction. A single empirical Green's function (EGF) is extracted between any two receivers in the array, thus there is no array processing performed. Active sources with similar geometries have been used elsewhere as a guide source to reduce the environment effects.<sup>22</sup> This is contrary to the approach taken here where unknown details of the propagation region are actually included in the EGF estimate.

To understand the salient features of EGF extraction in relation to the environment and source/receiver geometry, it is analyzed in Sec. II using ray theory and stationary phase. Although a homogeneous medium is assumed in the theory, the stationary phase argument does generalize to a heterogeneous medium, which may include varying sound speed profiles (SSPs),<sup>19</sup> as well as range dependent characteristics. Wavenumber integration<sup>23</sup> is used in Sec. III for the accurate modeling of the received waveforms in the experimental range independent environment.

<sup>a)</sup>Also at the School of Mechanical Engineering, University of Adelaide, Australia. Present address: Institute of Geophysics, Victoria University of Wellington, New Zealand. Author to whom correspondence should be addressed. Electronic mail: laura.brooks@vuw.ac.nz

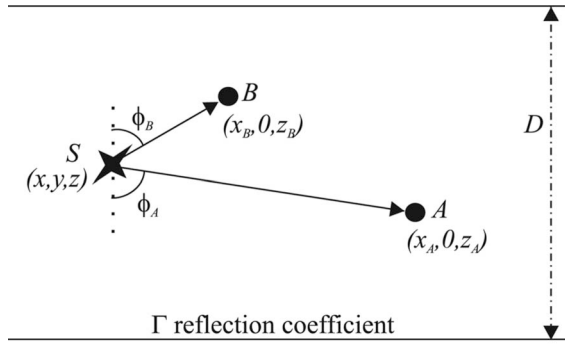


FIG. 1. Source-receiver geometry and notation. Receivers  $A$  and  $B$  define the  $y=0$  plane, and source  $S$  is located within the waveguide of depth  $D$ , but is otherwise unrestricted.

The Shallow Water 2006 (SW06) experiments provided an opportunity to collect experimental data on a single array of ocean hydrophones for both active and passive source OAI, and as such, provide a unique set of data for analysis and comparison of the different source types. In Sec. III, EGFs obtained using the two active source configurations (source lowering and towed source) are compared and contrasted with EGFs of noise emitted by the ship from which the source was lowered, and also with EGFs from a noise field dominated by waves and shipping. The active source experiments were performed in seas with 2–2.5 m swell, residual effects from the passing of a tropical storm the day before.<sup>6,24</sup> Although conditions hindered controllability of the experiments, and the extracted EGFs may have fluctuated more than usual, meaningful results were still obtained. The relative merits of different source types and receiver locations are evaluated through examination of the experimental results, and by relating these findings to the theory.

## II. BACKGROUND THEORY

Consider the isovelocity waveguide depicted in Fig. 1. The  $x$ ,  $y$ , and  $z$  directions are defined as the horizontal axis, the axis in-and-out of the page, and the vertical axis, respectively. Cross-correlation of the signals received at  $A$  and  $B$  from a source at  $S$  yields

$$C_{AB}(\omega) = \rho_s^2 |S(\omega)|^2 G(\mathbf{r}_A, \mathbf{r}_S) G^*(\mathbf{r}_B, \mathbf{r}_S), \quad (1)$$

where  $\omega$  is angular frequency,  $S(\omega)$  is the source spectrum,  $\rho_s$  is the density of the medium,  $G(\mathbf{r}_\psi, \mathbf{r}_S)$  is the Green's function between the source  $S$ , and receiver  $\psi$ , and  $*$  denotes the complex conjugate.

The sum of the cross-correlations over a set of sources is<sup>5,19</sup>

$$C_{AB}(\omega) = |\rho_s S(\omega)|^2 n \int G(\mathbf{r}_A, \mathbf{r}_S) G^*(\mathbf{r}_B, \mathbf{r}_S) dS, \quad (2)$$

where  $n$  is the number of sources per unit length (line source), area (planar source), or volume (volume source), and the integral is over the source line, plane, or volume.

In OAI, both the causal and acausal Green's functions,  $G(\mathbf{r}_A, \mathbf{r}_B)$  and  $G^*(\mathbf{r}_A, \mathbf{r}_B)$ , respectively, are extracted from the cross-correlation,  $C_{AB}(\omega)$ :

$$G(\mathbf{r}_A, \mathbf{r}_B) - G^*(\mathbf{r}_A, \mathbf{r}_B) = f(C_{AB}(\omega)). \quad (3)$$

If the source is only on one side of both  $A$  and  $B$ , then only the causal Green's function is extracted. The relating function  $f$  depends on the physical properties of the medium and the source distribution, as well as the dimension of the wave propagation. Its origin and form are explored here from a stationary phase perspective for four different source types:

- (1) active source lowered vertically over the depth of the waveguide at a location end-fire to the array, modeled as a vertical line of end-fire sources ( $\int dS \sim \int dz$ );
- (2) active source towed along the end-fire direction at a constant depth  $z$ , modeled as a horizontal line of sources at end-fire ( $\int dS \sim \int dx$ );
- (3) stationary ship source, modeled as an “extended” point source [ $\int dS \sim \int \delta(x, y) dS$ ]; and
- (4) ambient noise field, modeled as a horizontal plane of sources at a shallow depth  $z$  ( $\int dS \sim \iint dx dy$ ).

The first two cases, which are of main interest here, are described in Sec. II A. The two latter cases, which are included only for comparative purposes, are briefly described in Sec. II B.

### A. Cross-correlations for active sources

The phase of the integral term in Eq. (2) oscillates rapidly relative to the amplitude, and hence the integrand averages to almost zero except at points where its phase term is stationary (i.e., where the phase term has an extremum). The integrand can therefore be evaluated via the method of stationary phase; the integral is estimated in the neighborhood of the points where the phase term is stationary (at these locations the source is said to be located at a stationary point) and the contributions are then summed over all the stationary points. Stationary phase solutions to Eq. (2) have been derived elsewhere for various source configurations,<sup>5,19,21,25</sup> and hence full derivations are not presented here. The stationary phase solution assuming three-dimensional (3D)-wave propagation, for a vertical line of sources at end-fire, source type 1, is<sup>5</sup>

$$C_{AB}^1(\omega) = in |S(\omega)|^2 \sum_{z_{st}} \left( \frac{\Gamma^{b_{A,st}+b_{B,st}} \rho_s^2 G_f(R(z_{st}))}{\sin \phi_{st}} \sqrt{\frac{\xi(z_{st})c}{-8\pi i \omega}} \right), \quad (4)$$

and for a horizontal line of sources at end-fire, source type 2, is<sup>19,21</sup>

$$C_{AB}^2(\omega) = in |S(\omega)|^2 \sum_{x_{st}} \left( \frac{\Gamma^{b_{A,st}+b_{B,st}} \rho_s^2 G_f(R(x_{st}))}{\cos \phi_{st}} \sqrt{\frac{\xi(x_{st})c}{-8\pi i \omega}} \right), \quad (5)$$

where  $z_{st}$  and  $x_{st}$  are the vertical and horizontal end-fire stationary points, respectively,  $\Gamma$  is the bottom reflection coefficient,  $b_{\psi, st}$  is the number of bottom reflections for the path between the source  $S$ , located at stationary point  $p_{st}$  (either  $z_{st}$  or  $x_{st}$ ), and the receiver  $\psi$  (where  $\psi=A$  or  $B$ ),  $R(p_{st})$  is the difference in path lengths from the source, at  $p_{st}$ , to each of receivers  $A$  and  $B$ ,  $G_f(R) = e^{ikR}/4\pi R$  is the 3D Green's func-

tion within a homogeneous medium,  $\phi_{st}$  is the acute angle between the ray path and the vertical (see Fig. 1),  $\xi = (1/L_B) - (1/L_A)$ ,  $L_\psi$  is the length of the given path  $S$  and  $\psi$ , and  $c$  is the speed of sound in the medium. The 3D Green's function within a homogeneous medium,  $G_f(R)$ , differs from the true Green's function for a particular path between  $A$  and  $B$ ,  $C(R)$ , in that it does not incorporate the path dependent amplitude reduction due to bottom reflections:<sup>5</sup>

$$G(R(p_{st})) = \Gamma^{b_{st}} G_f(R(p_{st})), \quad (6)$$

where  $b_{st}$  is the number of bottom reflections for the arrival between  $A$  and  $B$  corresponding to the stationary point  $p_{st}$ . The solutions for the line sources, Eqs. (4) and (5) differ only in the trigonometric function of the acute ray angle ( $1/\sin \phi_s$  versus  $1/\cos \phi_s$ ), and the locations of stationarity.

The cross-correlation sums in Eqs. (4) and (5) are achieved experimentally by lowering a source through the water column ( $C_{AB}^1$ ), or towing it at end-fire to a hydrophone array ( $C_{AB}^2$ ), and then summing the cross-correlations throughout the period of source movement. An approximation to the Green's function, the EGF,  $g^{emp}$ , is then obtained from the cross-correlations:

$$g^{emp} = \sqrt{i\omega} C_{AB}^{obs}, \quad (7)$$

where  $C_{AB}^{obs}$  is either  $C_{AB}^1$  (vertical) or  $C_{AB}^2$  (horizontal). The sources are only on one side of the array, and hence only the causal part of the Green's function is approximated. The constants ( $n$ ,  $\rho_s$ ,  $c$ ,  $\pi$ , and numeric factors) and frequency dependent source term  $S(\omega)$  of Eqs. (4) and (5) can also be accounted for when comparing  $g^{emp}$  with the true Green's function, but path dependent factors ( $\Gamma^{b_A+b_B}$ ,  $\phi_s$ ,  $L_A$ , and  $L_B$ ) are more difficult to account for and are therefore neglected. Hence, the EGF obtained will not give correct amplitudes but should provide accurate arrival times.

Spurious arrivals, defined as peaks in the cross-correlation function at times not corresponding to Green's function path travel times, can occur for each source geometry. For the horizontal line configuration, spurious arrivals will result due to stationary phase contributions from cross-correlations between waves that initially undergo a surface reflection and ones that do not (for an isovelocity water column, one wave departs at an angle of  $\phi$  from the horizontal, and the other departs at an angle of  $-\phi$ ).<sup>3</sup> If the source is close to the sea surface, the spurious peaks converge to the same time delay as the true Green's function paths; however, they are  $\pi$  out of phase and will therefore result in shading of the Green's function.<sup>3</sup> For the vertical line configuration, spurious arrivals will result when the line integral does not extend from the sea surface through the ocean and underlying sediments to the acoustic penetration depth.<sup>5</sup>

## B. Stationary ship and ambient noise

For a point source (source type 3), Eq. (2) simplifies to

$$C_{AB}^3(\omega) = \frac{|\rho S(\omega)|^2 \Gamma^{b_A+b_B} e^{ik(L_A-L_B)}}{16\pi^2 L_A L_B}. \quad (8)$$

In general  $L_A - L_B$  is less than the inter-receiver path length and therefore arrival times are underestimated. Although the

stationary ship source is larger than a point source, the area of integration in Eq. (2) is small, and therefore it is not a true Green's function estimate. However, if the ship is close to a stationary path it may provide a good approximation of that path:

$$g^{emp} = C_{AB}^{obs}, \quad (9)$$

where  $C_{AB}^{obs}$  is  $C_{AB}^3$ . For a particular path  $p$ , as the ship approaches the corresponding stationary point, the component of the EGF corresponding to path  $p$  approaches the path  $p$  component of the Green's function between  $A$  and  $B$ .

Ship noise cross-correlations will only converge to the arrival structure of the Green's function when averaged over several ship tracks, hence the consideration of ship and wave dominated ambient noise (source type 4). For a horizontal plane of sources the stationary phase solution to Eq. (2) is (Refs. 3 and 6)

$$C_{AB}^4(\omega) = in |S(\omega)|^2 \sum_{\chi_{st}} \left( \frac{\Gamma^{b_{A,st}+b_{B,st}} c \rho_s}{2\omega \cos \phi_{st}} G_f(R(\chi_{st})) \right), \quad (10)$$

where  $\chi_{st}$  are the horizontal planar stationary points and all other parameters are the same as for Eqs. (4) and (5).

Since this source distribution surrounds the hydrophones, both the causal and acausal Green's functions are approximated:

$$g^{emp} - g^{emp*} = \omega C_{AB}^{obs}. \quad (11)$$

## III. EXPERIMENT

### A. Data collection

The SW06 experiments were an Office of Naval Research sponsored set of low and medium frequency acoustic experiments conducted off the northeast coast of the United States. The acoustic data considered here were collected on an L-shaped array [geometry shown in Fig. 2(a)] located in water approximately 70 m deep. This allowed for many hydrophone pair geometries. Hydrophones 1–10 (H-1–H-10) constituted the vertical line array (VLA). They were evenly spaced at 5.95 m intervals, the lowest, H-10, being 4.65 m above the seafloor. H-13–H-32 constituted the 256.43 m long seafloor mounted horizontal line array (HLA). H-13 was located 7.795 m from the VLA. Spacing between subsequent HLA hydrophones decreased from 20.32 m at this end to 8.33 m at the array tail.

Data from four source types were recorded:

- (1) 1200–2900 Hz one second duration continuous linear frequency modulated (LFM) signal emitted by an omnidirectional source lowered from 9.8–60 m at a constant rate of 1 m/min, at a location 466 m from the VLA, in the end-fire plane [see source lowering geometry and location in Figs. 2(a) and 2(b)];
- (2) 1200–2900 Hz one second duration continuous LFM signal emitted by an omnidirectional source held at 10 m depth towed at 1 kn toward the array in the end-fire plane, from a distance of 1.5 km from the VLA, to a location mid-way between H-16 and H-30 [see towed source geometry and location in Figs. 2(a) and 2(b)];

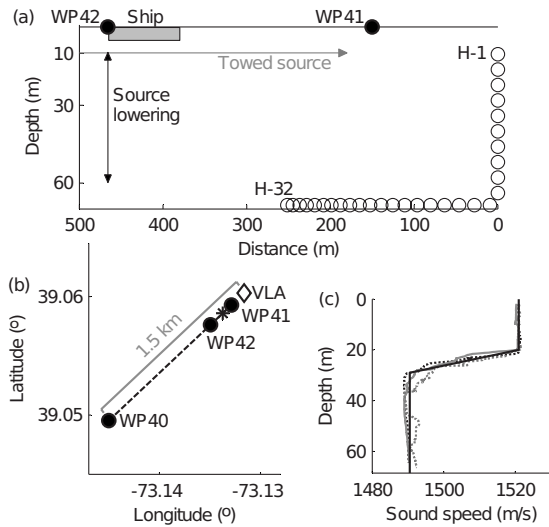


FIG. 2. (a) Source and receiver geometries: array hydrophones shown as circles, and ship location is during source lowering. (b) Plan view of array (VLA labeled, asterisk marks far end of HLA) and source geometries (source towed from WP40 to WP41, and lowered at WP42). (c) SSPs from CTDs 42–44 (black dotted, gray solid, and gray dotted lines, respectively), and assumed SSP for modeling (black solid line).

- (3) 20–100 Hz noise generated by the deployment vessel *R/V Knorr* [location shown in Fig. 2(a)] during the source lowering experiment; and
- (4) 20–100 Hz ship and wave dominated ambient noise.<sup>6</sup>

The ship and wave dominated noise data, source type 4, were collected during tropical storm Ernesto over the entire day of September 2, and data from source types 1–3 were collected on the afternoon of September 3, 2006. There was little wind, but there was a residual swell of 2–2.5 m, as well as strong inhomogeneity in the ocean due to the previous day’s storm. These made it difficult to move the active source along the desired tracks. SSPs were recorded from three CTD-casts (conductivity, temperature, and depth) obtained before, during, and after the experiments on September 3, as shown in Fig. 2(c), along with a simpler SSP used for simulations. The September 2 storm would have increased mixing in the upper layer and hence the SSP would have changed throughout the day, the most noticeable aspect of which would have been the formation of a steeper thermocline. However, the adverse weather conditions meant that no CTD-casts could be obtained during this period. The September 2 data are therefore analyzed here using simulated travel times derived from the September 3 model SSP.

## B. Data analysis

Active source data from all hydrophone pairs were bandpass filtered to 1200–2900 Hz, and ship and wave noise data were bandpass filtered to 20–100 Hz. The ship and wave dominated ambient noise data were then one-bit normalized in the time domain (i.e., amplitude was discarded but sign, or phase, of the waveform was retained), bandpass filtered once again, and spectrally whitened by inversely weighting the frequency domain data with a smooth version of their amplitude spectra within the bandpass frequency.

The active source and stationary ship data did not require normalization since variations in the source amplitude and phase characteristics were negligible throughout each experiment.

The preprocessed data were cross-correlated over short time intervals, and then summed over the period of collection for each source type. As specified in Sec. II, a raw summed cross-correlation [see Eqs. (4), (5), and (10)] yields a phase and amplitude shaded Green’s function approximation. Corrections to the phase shading and frequency dependent components for source types 1 and 2 were made. Although source type 3 also has a phase shift, it is geometry dependent, due to the length discrepancy in the exponential of Eq. (8), and therefore no correction factors were applied. Inclusion of the appropriate phase correction is, henceforth, implicit in the term “cross-correlation.”

The cross-correlation sum corresponds to the EGF (see Sec. II). The normalized EGFs of the cross-correlations between H-30 and all other hydrophones are plotted in Fig. 3 overlying a pseudocolor plot of their envelopes for the four source types in Sec. III A. Simulated direct (D), surface reflected (S), surface-bottom reflected (SB, VLA only), and surface-bottom-surface reflected (SBS) path travel times, which were determined using OASES,<sup>23</sup> are overlaid as dash-dotted lines for comparison. The simulations use the simplified SSP of Fig. 2(c), and assume a 20 m deep sediment layer ( $c=1650$  m/s,  $\alpha=2.7$  dB/ $\lambda$ ,  $\rho=1.85$  g/cm<sup>3</sup>) overlying a basement ( $c=1900$  m/s,  $\alpha=2.0$  dB/ $\lambda$ ,  $\rho=2.0$  g/cm<sup>3</sup>). These geoacoustic parameters, inferred at the active source frequencies from geoacoustic inversion results at the array site,<sup>26</sup> correspond to a critical angle of 25°. Lower values of the sediment attenuation, which would be expected in the general region<sup>27</sup> or at lower frequencies, show small peaks in the Green’s function corresponding to reflections from the sediment-basement interface (not shown).

The ship dominated ambient noise results, as shown in Fig. 3(d), have both causal and acausal components because the sound comes from all directions, though only the first 0.05 s of the acausal signal is shown here. Results from the other three configurations, shown in Figs. 3(a)–3(c), have sound traveling in one direction only, left to right from the perspective of Fig. 2(a), and therefore produce a one-sided EGF. The stationary ship EGF, (c), and ship and wave dominated ambient noise EGF, (d), show broader peaks than the active source results, (a) and (b), due to the lower frequencies of the ship (20–100 Hz compared to the 1200–2900 Hz active source frequencies).

The EGF envelopes for all source types, as shown in Fig. 3, exhibit distinct peaks at times agreeing with the simulated direct inter-hydrophone travel times. The times corresponding to these peaks are compared in Fig. 4(a). Simulated travel times are subtracted from these times, and the resulting time differences are shown in Fig. 4(b). Minimal variations are seen for all HLA hydrophone combinations, though the stationary ship peak time differences (c) are generally greater than the others, which is due to the discrete nature of the source location; no signals from the source pass through

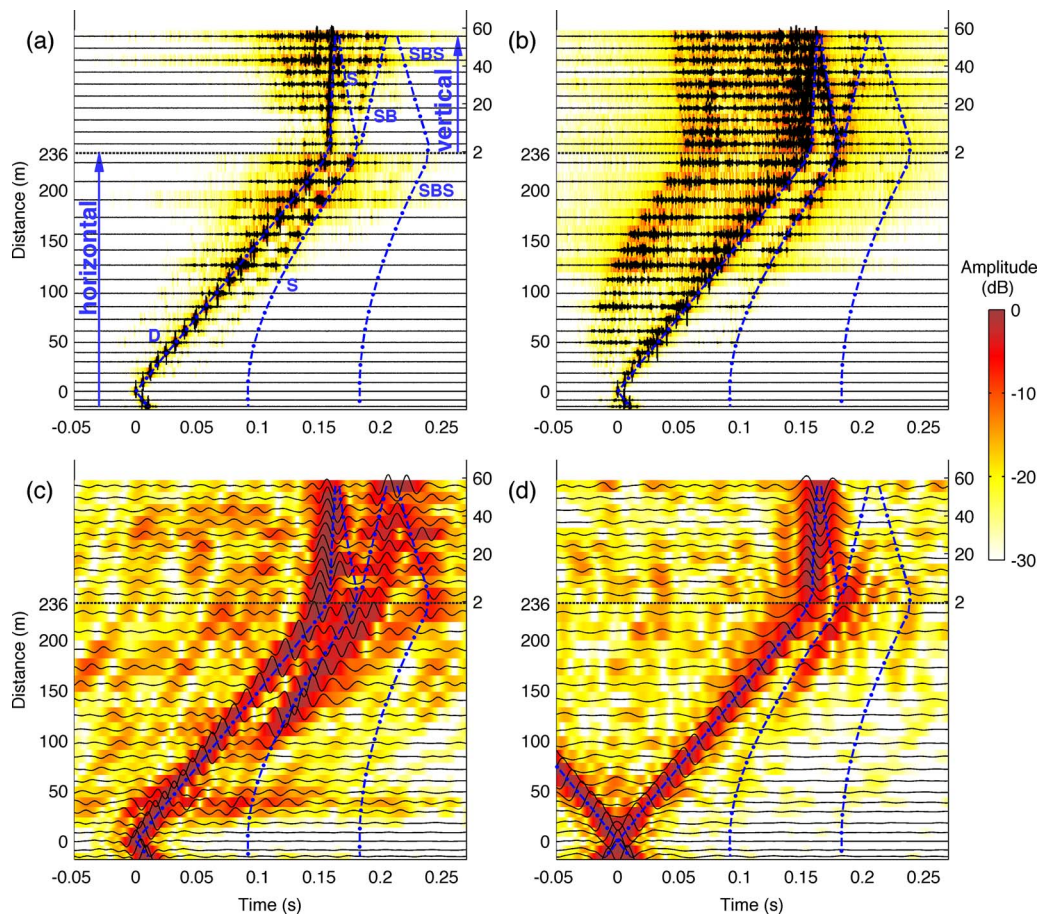


FIG. 3. (Color online) EGFs (black, normalized to their maximum value) between H-30 and all other hydrophones overlying pseudocolor plots of their envelopes (dB relative to maximum value) for (a) source lowering, (b) towed source, (c) stationary ship, and (d) causal ambient noise. The lower traces (below the dashed line) are from cross-correlations with HLA hydrophones; their distance from H-30 is on the left axis. The upper traces are from cross-correlations with VLA hydrophones; their vertical distance from the seafloor is on the right axis. The dash-dot lines are simulated travel times.

the location of the first hydrophone, on their way to the second hydrophone, with a direct path in between.

The variation in the EGF peak times corresponding to the direct arrivals between the hydrophones are notably larger for the VLA. Due to their location, the VLA hydrophones are more sensitive to environmental variations and more susceptible to movement than their HLA counterparts.

The EGF peaks corresponding to the surface reflected arrivals in Fig. 3 show more variation than the direct path peaks, but due to the lower grazing angles, are consistently more accurate for hydrophones with a greater horizontal separation. The towed source and ambient noise results, shown in Figs. 3(b) and 3(d), respectively, show a surface reflection peak for all ranges larger than 40 m from H-30. The source lowering, shown in Fig. 3(a), exhibit peaks at slightly early times for ranges larger than 150 m from H-30. For ranges less than 150 m, peak times diverge from the simulated values. The stationary ship results, shown in Fig. 3(c), show an arrival peak for ranges greater than 100 m, but the VLA arrivals are less clear.

The amplitudes of the EGF peaks are greatest, relative to the background noise, for the active source cross-correlations. This is due to high levels of coherently propagating noise which result from the close proximity of the source and the even distribution of the source over the active

source line integrals. Unlike the other source configurations, the towed source results in Fig. 3(b) show a peak in the EGF at an arrival time earlier than the direct path for all distances. The reason for this apparent early arrival is explained in Sec. III B 2.

To explain the features of the EGFs of Fig. 3, OAI data for one hydrophone pair, H-30 and H-5, will be examined in detail for each source type in the coming sections.

### 1. Source lowered vertically

The theoretical vertical line source description in Sec. II assumes a set of sources that is uniformly distributed along the line.<sup>5</sup> The single source used here was slowly lowered, but was only at one location at any time. The line source configuration was therefore obtained by cross-correlating data over short time intervals and summing these cross-correlations. Thus, while the cross-correlations over depth are described here, it is only the summed cross-correlations which are used to approximate the EGF. This EGF approximation could instead have been implemented as one large cross-correlation.

The geometry of the source lowering, as well as the stationary point travel paths and surface and bottom sources that converge to the stationary points for H-5 and H-30, are

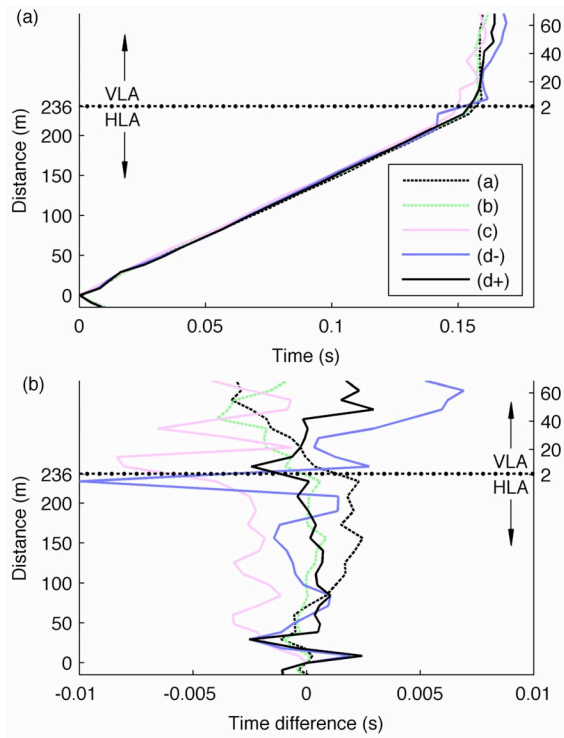


FIG. 4. (Color online) (a) Travel times corresponding to the direct path arrival EGF envelope peaks of Fig. 3 as a function of hydrophone number, and (b) differences between these and the simulated travel times. Legend: (a) source lowering, (b) towed source, (c) stationary ship, (d+) causal ambient noise, and (d-) acausal ambient noise.

shown in Fig. 5. Ideally a source should be lowered through the water column and sediment,<sup>5,19</sup> but due to experimental restrictions the source could only be lowered from 9.8–60 m (8.5 m above the seafloor).

Correlation gathers of 100 s duration between H-5 and

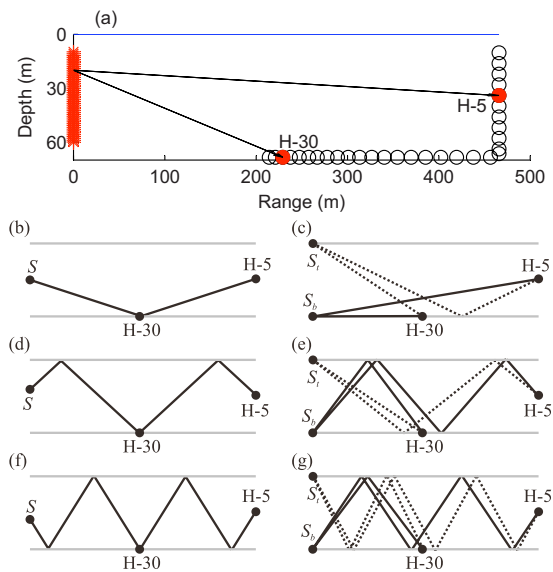


FIG. 5. (Color online) Source lowering. (a) Source (far left) is lowered from 9.8–60 m, and signals are recorded on H-5 and H-30 (solid circles). (b)–(g) Source-receiver geometry and stationary point paths for (b) direct, (d) surface, and (f) surface-bottom paths. (c), (e), and (g) are the surface ( $S_t$ ) and bottom ( $S_b$ ) source to receiver paths that converge to the stationary point paths in (b), (d), and (f), respectively.

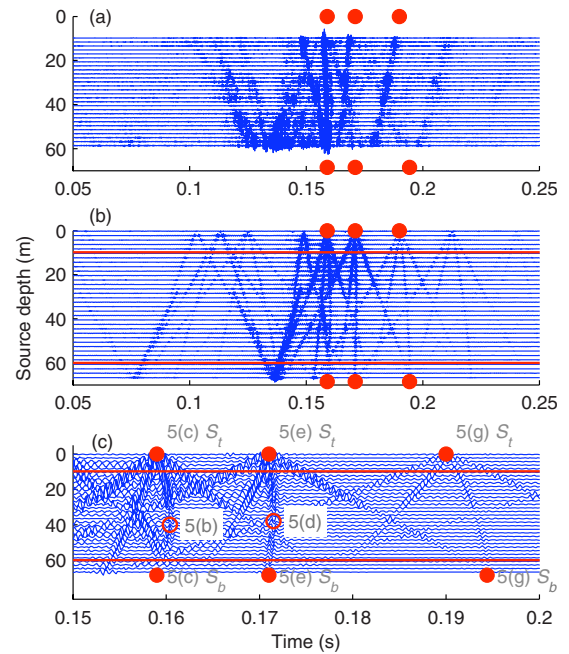


FIG. 6. (Color online) Correlation gathers for source lowering: (a) experimental, (b) simulated, and (c) extract of simulated data. The solid circles correspond to time differences between the surface and bottom source paths to H-5 and H-30 [Figs. 5(c), 5(e), and 5(g)], and the transparent circles in (c) correspond to the direct and surface reflection stationary points in Figs. 5(b) and 5(d).

H-30 are shown as a function of depth for experimental data in Fig. 6(a), and data simulated using OASES in Figs. 6(b) and 6(c). Cross-correlation peaks occur at the time differences between paths from the source to each hydrophone. The direct path between H-30 and H-5 is extracted from the cross-correlation of the direct path from the source to H-30 and the bottom reflected path to H-5 [see Figs. 5(b) and 5(c)]. The simulated time differences between these paths for sources at the top or bottom of the waveguide [Fig. 5(c)] are depicted in Fig. 6 as the first set of solid circles (0.16 s). The curve of maxima connecting these circles corresponds to the time difference between these paths for each source depth. The time difference increases to a stationary point at ~40 m depth [circle in Fig. 6(c)]. This stationary point occurs when the path to the second hydrophone (H-5) passes through the first hydrophone (H-30) [Fig. 5(b)]; i.e., the two paths have a travel time difference equivalent to the direct arrival between H-30 and H-5.

The surface and surface-bottom reflected arrivals between two hydrophones can be analyzed similar to the direct arrival as shown in Fig. 5 and marked with circles in Fig. 6.

Contributions to the EGF at the surface and bottom will generally cancel. Consider the four paths that converge at the surface of the waveguide to the direct path to H-30 and bottom reflected to H-5 [first circle (c)  $S_t$  in Fig. 6(c)], as shown in detail with schematics of the paths that converge to this point in Fig. 7. The cross-correlations of paths (b) and (e) are in phase (one surface reflection each) and their amplitudes are equal in amplitude at the convergence point. Since the path length difference of (b) increases towards the surface, and that of (e) decreases towards the surface, and their rates of change are also the same, the cross-correlation peaks due

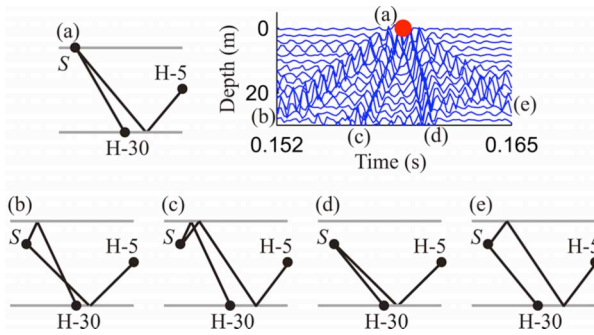


FIG. 7. (Color online) Close-up view of the simulated correlation gathers [Fig. 6(c)], showing the direct path to H-30 and bottom reflected to H-5 surface convergence point (a), and the four sets of paths that converge to this point (b)–(e).

to these combinations transfer smoothly from one path combination to the other, and therefore there is no spurious arrival. A similar argument holds for other sets of paths at the surface and bottom [including paths (c) and (d) in Fig. 7], and therefore there is generally no peak in the summed cross-correlations at these convergence points. Exceptions to this generality can occur when the total number of surface and bottom reflections of the two converging paths are not identical. Since the amplitude of the surface and bottom reflections coefficients is generally less than unity, one of the converging paths will likely be stronger than the other, creating a residual peak in the cross-correlation at this point. The amplitude of this peak will often be negligible, but sometimes it will be large enough to have an impact on the results, as will be shown for two convergence points in the experimental data here.

The simulated and experimental data of Fig. 6 differ in three ways:

- (1) The experimental data are less sharp, likely due to meter high waves, which caused both the source and waveguide depth to oscillate.
- (2) There are variations in amplitudes for different path combinations, with some path combinations more affected than others. Likely reasons are that the bottom reflection coefficient, or sediment properties, of the simulation are only an estimation, and that due to ocean waves, the angle of the surface reflected signal (relative to horizontal) would be time dependent and the signal would be scattered. Most paths depend on some power of surface and bottom reflection, see Eqs. (4)–(10), and higher order paths are more sensitive to these reflection coefficients.
- (3) Peak times differ slightly, likely due to slight mismatch in SSP and water column depth between the experimental and simulated environments.

The amplitude differences between the simulated and experimental data (item 2) could potentially be used to invert for surface and bottom reflection.

Having constructed the cross-correlation at each point in depth, the EGF can then be extracted by summing these contributions.<sup>3,5,19</sup> The cross-correlations were summed over depth and the resulting EGFs are compared with both simu-

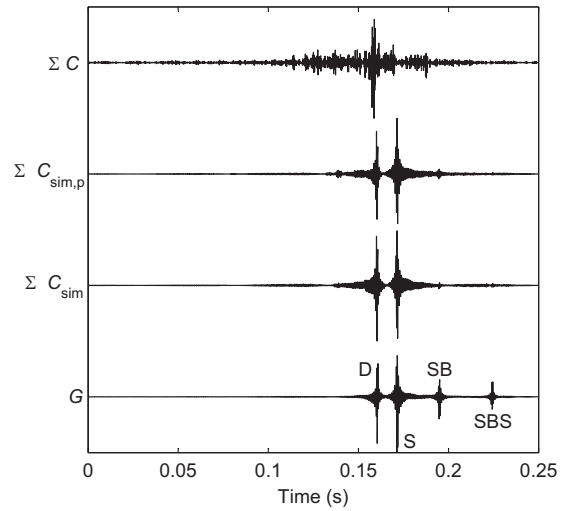


FIG. 8. H-5 to H-30 EGF from the source lowering experiment ( $\Sigma C$ ) is compared to the simulated cross-correlations summed from 9.8–60 m ( $\Sigma C_{sim,p}$ ), the simulated cross-correlations summed over the entire waveguide ( $\Sigma C_{sim}$ ), and the simulated source shaded Green's function ( $G$ ). Green's function shows direct (D), surface (S), surface-bottom (SB), and surface-bottom-surface (SBS) paths.

lated summed data and the source shaded Green's function in Fig. 8. The sum of the simulated data over the waveguide,  $\Sigma C_{sim}$ , shows direct, surface reflected, and surface-bottom reflected peaks at correct Green's function,  $G$ , time lags. The amplitudes are different, as explained in Sec. II. The significantly smaller amplitude of the surface-bottom reflected path in  $\Sigma C_{sim}$  when compared to the Green's function is due to losses from the many boundary interactions. The Green's function for this path has only one surface and one bottom reflection, but the two paths that are cross-correlated have three surface and four bottom reflections between them [see Eqs. (4) and (6)]. The sum of the simulated data from 9.8–60 m only,  $\Sigma C_{sim,p}$ , has small spurious peaks at  $\sim 0.14$  s, which is earlier than the direct arrival. These are due to the 8.5 m gap in cross-correlations at the waveguide bottom.

While the experimental data matches well the direct arrival, both the surface and surface-bottom reflected arrivals appear early in Figs. 3 and 8. This is because in the experimental cross-correlation [Fig. 6(a)], complete cancellation at the near surface cross-correlation endpoints (second and third solid circles) does not occur. The amplitude of the surface reflection coefficient is likely less than unity, resulting in one arrival dominating and therefore contributions near the surface convergence points (circles in Fig. 6).

## 2. Source towed horizontally

Following the same reasoning as with the source lowering (Sec. III B 1), short time cross-correlations were summed as the source was towed from WP40 to WP41. Tapering was incorporated to cross-correlations near WP40 to minimize end-effects. Ideally the ship would have continued past WP41, over the VLA and 1.5 km further, with tapering at both ends; however, the ship had to stop at WP41 as it could not sail above the VLA. Tapering at this endpoint is difficult as this reduces the amplitudes of nearby stationary points.

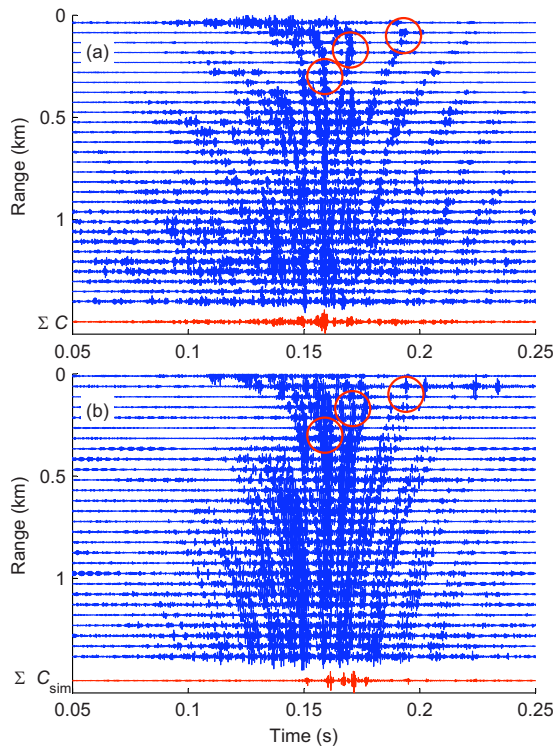


FIG. 9. (Color online) Towed source correlation gathers: (a) experimental and (b) simulated data, as a function of range (0–1.4 km) from H-30. The summed cross-correlations  $\Sigma C$  and  $\Sigma C_{sim}$  are at the bottom of each plot.

The cross-correlations at this endpoint are visible in Fig. 3(b) as peaks in amplitude at times less than 0.05 s corresponding to the path length difference to each hydrophone at this point. These times are significantly less than the expected arrival times of D, S, and B.

The H-5 and H-30 100 s long correlation gathers are shown in Fig. 9 as a function of range for experimental data, and data simulated using OASES. The direct, surface reflection, and surface-bottom reflection stationary points (the turning points where the travel time for an arrival is a maximum) are circled. The corresponding stationary phase paths are shown in Figs. 10(a)–10(c). The stationary points occur within the first few hundred meters; the cross-correlation peak times increase rapidly in range to these points (Fig. 9),

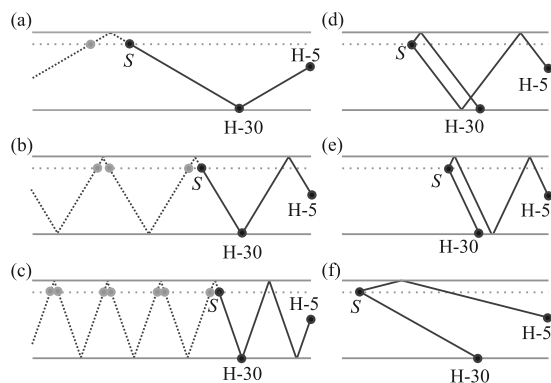


FIG. 10. (a)–(c) Source-receiver geometry and stationary point paths for (a) direct path, (b) surface reflection path, and (c) surface-bottom reflection path. The gray circles represent weaker stationary points. (d)–(f) Stationary phase geometries that yield spurious arrivals.

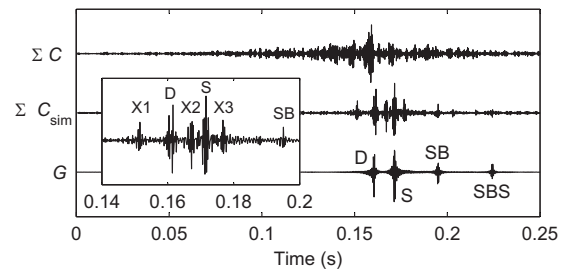


FIG. 11. H-5 to H-30 EGF from the toward source experiment ( $\Sigma C$ ) is compared to the simulated summed cross-correlations ( $\Sigma C_{sim}$ ), and the simulated source shaded H-5 to H-30 Green's function ( $G$ ). Green's function shows direct (D), surface (S), surface-bottom, (SB) and surface-bottom-surface (SBS) paths. An enlarged view of  $\Sigma C_{sim}$  from 0.14–0.2 s, showing inter-hydrophone (D, S, and SB) and spurious (X1–X3) arrivals, is inset.

and then asymptote towards a far-field fixed value. Higher multiples [gray in Figs. 10(a)–10(c)] also yield stationary points, but due to increased boundary interactions, their amplitudes are much smaller, and are not visible in Fig. 9.

The H-5 to H-30 EGF for the source towed horizontally (the experimental cross-correlations summed over range),  $\Sigma C$ , is compared in Fig. 11 with the simulated summed cross-correlations,  $\Sigma C_{sim}$ , and the simulated source shaded Green's function,  $G$ . The simulated cross-correlation sum shows direct (D), surface reflected (S), and surface-bottom (SB) arrival peaks at correct lag times. The experimental data have stationary points [Fig. 9(a)] that yield arrival peaks (Fig. 11) at times slightly less than the simulated direct and surface reflected arrivals. This is likely due to mismatch between the experimental and simulated water depths and SSPs. The experimental summed cross-correlation also has a higher noise level, which is likely due to convergence difficulties near zero range, where the data are sensitive to tapering and the chosen physical endpoint.

Both the experimental and simulated cross-correlation sums exhibit numerous high amplitude spurious arrivals. For example, consider the two spurious arrivals (X2) and (X3) that are visible in the summed simulated cross-correlations (Fig. 11) before and after the surface reflected arrival (S). These are the result of stationary points corresponding to non-Green's function arrivals [paths in Figs. 10(d) and 10(e)], as explained in Sec. II.

The arrivals and stationary points that create these peaks are visible in Fig. 9(b). Peaks corresponding to the time difference in the direct path to H-30 and the bottom-surface reflected path to H-5 (with the surface reflection stationary point at 0.17 s circled) are flanked by a set of arrivals at slightly earlier and later times. These additional arrivals, which are due to the cross-correlation of a wave which initially undergoes a surface reflection with one that does not, have stationary points corresponding to the geometry of Figs. 10(d) and 10(e), and hence the spurious arrivals (X2) and (X3) are apparent in the summed cross-correlations of Fig. 11.

A significant peak (X1) is apparent in both the experimental and simulated cross-correlations at 0.15 s, prior to the direct path (D) arrival. This spurious arrival is due to a stationary phase contribution from the cross-correlation of the direct path to H-30 and surface reflection to H-5 [Fig. 10(f)].

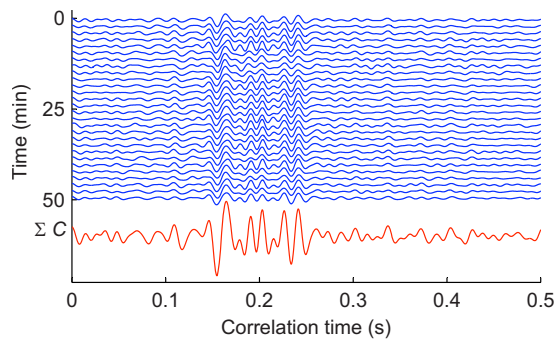


FIG. 12. (Color online) H-30 to H-5 EGFs from stationary ship data as a function of time during the source lowering event. The summed EGF ( $\Sigma C$ ) is shown underneath.

The peaks in the simulated and experimental data exist only in this varying SSP environment. Simulated cross-correlations (not shown) for an isovelocity (1500 m/s) waveguide with the same geometry do not show this peak, because such a stationary phase geometry does not exist when considering straight line paths only [the schematic of straight line paths in Fig. 10(f) comes close to, but does not satisfy, the equal departure angle requirement; the path to H-5 always departs the source at an angle closer to the horizontal than the path to H-30].

### 3. Stationary ship noise and ambient noise

The cross-correlated data from the stationary ship varied little with time (see Fig. 12). Due to the crude approximation, a good estimate of the Green's function is not expected. Cross-correlation of the ship data during this time yields a multi-path result that looks similar to the Green's function, however the arrival *structure* will have path dependent inaccuracies. The times tend to be a little early due to stationary phase paths not all being sampled by the small ship source volume.

The structure of ship cross-correlations will only converge to that of the true Green's function if either the ship moves along the end-fire direction or the cross-correlations are averaged over many ship tracks that intersect the end-fire direction. Ship dominated ambient noise, which has been investigated in detail for the same data elsewhere,<sup>6</sup> will not be discussed further here.

## IV. CONCLUSION

It has been demonstrated theoretically and experimentally that the EGF between two receivers can be extracted from active sources. The EGF is determined by summing the cross-correlations between the receivers over all source positions. Here a source was lowered vertically through the water column, and also towed horizontally at shallow depth.

EGFs determined from two active source configurations, a vertically lowered source and a horizontally towed source, were compared with EGFs from a stationary ship at a single end-fire location, and EGFs from a ship/wave dominated ambient noise field. It has been shown that the EGFs from all source configurations yield direct arrival time estimates that

match well with the simulated travel times. However, the stationary ship arrival times were slightly early because it is only an extended point source.

The horizontal tow results exhibited high noise levels at times prior to the direct arrival. This noise would be greatly reduced if the towed source were extended past the array. For the source lowered vertically had lower noise levels, but surface and surface-bottom paths were not as well determined. Lowering over the entire water column depth would improve the result, as would calmer sea conditions; however, due to difficulties sampling near the surface and bottom as well as with penetrating the sediment, higher order paths would still not be retrieved as well as they are for the horizontally towed source, which shows more overall potential. If instead of a single source that is moved along a line, or a line of multiple sources (vertical or horizontal) were used simultaneously, then the problem of a changing environment could be ameliorated. This could potentially be advantageous over the ambient noise methods, which although they are sound in most other aspects, suffer from needing data collection over a time window larger than the time-scale of some environmental changes, which results in them providing an estimate of a time-averaged rather than instantaneous Green's function.

Active source OAI can potentially be used to construct new propagation paths between the receivers, which can then be used for inferring the medium between these paths. To make this practical, it is important to understand the sources of error and to take these into account when designing future experiments. In particular, elimination of spurious arrivals and reducing arrival time bias are important for developing active source methods further.

## ACKNOWLEDGMENTS

Work supported by the Office of Naval Research under Grant No. N00014-05-1-0264. L.A.B. is appreciative of support from a Fulbright Postgraduate Award in Science and Engineering, sponsored by Clough Engineering, as well as support from the Defence Science and Technology Organisation, Australia.

<sup>1</sup>P. Roux and M. Fink, "Green's function estimation using secondary sources in a shallow water environment," *J. Acoust. Soc. Am.* **113**, 1406–1416 (2003).

<sup>2</sup>P. Roux, W. A. Kuperman, and the NPAL Group, "Extracting coherent wave fronts from acoustic ambient noise in the ocean," *J. Acoust. Soc. Am.* **116**, 1995–2003 (2004).

<sup>3</sup>K. G. Sabra, P. Roux, and W. A. Kuperman, "Arrival-time structure of the time-averaged ambient noise cross-correlation function in an oceanic waveguide," *J. Acoust. Soc. Am.* **117**, 164–174 (2005).

<sup>4</sup>K. G. Sabra, P. Roux, A. M. Thode, G. D'Spain, W. S. Hodgkiss, and W. A. Kuperman, "Using ocean ambient noise for array self-localization and self-synchronization," *IEEE J. Ocean. Eng.* **30**, 338–347 (2005).

<sup>5</sup>L. A. Brooks and P. Gerstoft, "Ocean acoustic interferometry," *J. Acoust. Soc. Am.* **121**, 3377–3385 (2007).

<sup>6</sup>L. A. Brooks and P. Gerstoft, "Green's function approximation from cross-correlations of 20–100 Hz noise during a tropical storm," *J. Acoust. Soc. Am.* **125**, 723–734 (2009).

<sup>7</sup>R. L. Weaver and O. I. Lobkis, "Ultrasonics without a source: Thermal fluctuation correlations at MHz frequencies," *Phys. Rev. Lett.* **87**, 134301 (2001).

<sup>8</sup>P. Roux, K. G. Sabra, W. A. Kuperman, and A. Roux, "Ambient noise cross correlation in free space: Theoretical approach," *J. Acoust. Soc. Am.* **117**, 79–84 (2005).

- <sup>9</sup>N. M. Shapiro, M. Campillo, L. Stehly, and M. H. Ritzwoller, "High-resolution surface-wave tomography from ambient seismic noise," *Science* **307**, 1615–1618 (2005).
- <sup>10</sup>P. Gerstoft, K. G. Sabra, P. Roux, W. A. Kuperman, and M. C. Fehler, "Green's functions extraction and surface-wave tomography from microseisms in southern California," *Geophysics* **71**, SI23–SI31 (2006).
- <sup>11</sup>K. Wapenaar and J. Fokkema, "Green's function representations for seismic interferometry," *Geophysics* **71**, SI33–SI46 (2006).
- <sup>12</sup>F. Lin, M. H. Ritzwoller, J. Townend, S. Bannister, and M. K. Savage, "Ambient noise Rayleigh wave tomography of New Zealand," *Geophys. J. Int.* **170**, 649–666 (2007).
- <sup>13</sup>Y. Yang, M. H. Ritzwoller, A. L. Levshin, and N. M. Shapiro, "Ambient noise Rayleigh wave tomography across Europe," *Geophys. J. Int.* **168**, 259–274 (2007).
- <sup>14</sup>E. Larose, A. Khan, Y. Nakamura, and M. Campillo, "Lunar subsurface investigated from correlation of seismic noise," *Geophys. Res. Lett.* **32**, L16201 (2005).
- <sup>15</sup>K. G. Sabra, S. Conti, P. Roux, and W. A. Kuperman, "Passive *in vivo* elastography from skeletal muscle noise," *Appl. Phys. Lett.* **90**, 194101 (2007).
- <sup>16</sup>O. A. Godin, "Retrieval of Green's functions of elastic waves from thermal fluctuations of fluid-solid systems," *J. Acoust. Soc. Am.* **125**, 1960–1970 (2009).
- <sup>17</sup>G. A. Prieto and G. C. Beroza, "Earthquake ground motion prediction using the ambient seismic field," *Geophys. Res. Lett.* **35**, L14304 (2008).
- <sup>18</sup>S. R. Taylor, P. Gerstoft, and M. C. Fehler, "Estimating site amplification factors from ambient noise," *Geophys. Res. Lett.* **36**, L09303 (2009).
- <sup>19</sup>R. Snieder, K. Wapenaar, and K. Larner, "Spurious multiples in seismic interferometry of primaries," *Geophysics* **71**, SI111–SI124 (2006).
- <sup>20</sup>D. Mikesell, K. van Wijk, A. Calvert, and M. Haney, "The virtual refraction: Useful spurious energy in seismic interferometry," *Geophysics* **74**, A13–A17 (2009).
- <sup>21</sup>R. Snieder, "Extracting the Green's function from the correlation of coda waves: A derivation based on stationary phase," *Phys. Rev. E* **69**, 046610 (2004).
- <sup>22</sup>M. Siderius, D. R. Jackson, D. Rouseff, and M. R. Porter, "Multipath compensation in shallow water environments using a virtual receiver," *J. Acoust. Soc. Am.* **102**, 3439–3449 (1997).
- <sup>23</sup>H. Schmidt, *OASES Version 3.1 User Guide and Reference Manual*, Department of Ocean Engineering, Massachusetts Institute of Technology (2004).
- <sup>24</sup>J. Traer, P. Gerstoft, P. D. Bromirski, W. S. Hodgkiss, and L. A. Brooks, "Shallow-water seismoacoustic noise generated by tropical storms Ernesto and Florence," *J. Acoust. Soc. Am.* **124**, EL170–EL176 (2008).
- <sup>25</sup>K. G. Sabra, P. Gerstoft, P. Roux, and W. A. Kuperman, "Extracting time-domain Green's function estimates from ambient seismic noise," *Geophys. Res. Lett.* **32**, L03310 (2005).
- <sup>26</sup>D. P. Knobles, P. S. Wilson, J. A. Goff, and S. E. Cho, "Seabed acoustics of a sand ridge on the New Jersey continental shelf," *J. Acoust. Soc. Am.* **124**, EL151–EL156 (2008).
- <sup>27</sup>Y.-M. Jiang, N. R. Chapman, K. Yang, and Y. Ma, "Estimating marine sediment attenuation at low frequency with a vertical line array," *J. Acoust. Soc. Am.* **125**, EL158–EL163 (2009).